MATERIALS SCIENCE

Enhanced transport in transistor by tuning transition-metal oxide electronic states interfaced with diamond

Zongyou Yin[1,2]*, Moshe Tordjman[1,3]*†, Youngtack Lee[1], Alon Vardi[1], Rafi Kalish[3], Jesús A. del Alamo[1]†

High electron affinity transition-metal oxides (TMOs) have gained a central role in two-dimensional (2D) electronics by enabling unprecedented surface charge doping efficiency in numerous exotic 2D solid-state semiconductors. Among them, diamond-based 2D electronics are entering a new era by using TMOs as surface acceptors instead of previous molecular-like unstable acceptors. Similarly, surface-doped diamond with TMOs has recently yielded record sheet hole concentrations (2×10^{14} cm^{-2}) and launched the quest for its implementation in microelectronic devices. Regrettably, field-effect transistor operation based on this surface doping has been so far disappointing due to fundamental material obstacles such as (i) carrier scattering induced by nonhomogeneous morphology of TMO surface acceptor layer, (ii) stoichiometry changes caused by typical transistor fabrication process, and (iii) carrier transport loss due to electronic band energy misalignment. This work proposes and demonstrates a general strategy that synergistically surmounts these three barriers by developing an atomic layer deposition of a hydrogenated MoO$_3$ layer as a novel efficient surface charge acceptor for transistors. It shows high surface uniformity, enhanced immunity to harsh fabrication conditions, and benefits from tunable electronic gap states for improving carrier transfer at interfaces. These breakthroughs permit crucial integration of TMO surface doping into transistor fabrication flows and allow outperforming electronic devices to be reached.

INTRODUCTION

The growing demands for electronic devices with higher performance in power, frequency, energy efficiency, and a lower form factor are driving the need to find alternative functionalization of novel semiconductors with more desirable intrinsic properties. In some of the newly discovered semiconductors, more efficient and simplified doping methods such as charge-transfer doping are becoming prevalent (1). Surface transfer doping (STD) was invoked first (2, 3) in an effort to unravel the unexpected p-type surface conductivity of intrinsic diamond. It has since quickly become a widely used scheme for high-efficiency doping of semiconductors (4–9).

STD occurs when electrons from the valence band of diamond transfer toward unoccupied states of a surface acceptor adsorbed at the surface, giving rise to a subsurface two-dimensional hole gas (2DHG) (3, 9). Diamond, considered as a next-generation semiconductor material because of its outstanding physical, thermal, and electronic properties (10), benefits from a negative electron affinity property associated with its hydrogen-terminated surface (diamond:H) that facilitates STD (11–13). The resulting 2DHG channel can be exploited to implement diamond-based electronic devices. Toward the goal of enhancing the 2DHG stability and conductivity, tremendous efforts have recently been dedicated to exploring novel surface acceptor materials.

STD on diamond:H was first demonstrated using molecular-like surface acceptors with high electron affinity (14–17). This approach, however, suffers from instability to temperature and loss of conductivity upon heating (18). Alternatively, stability enhancement has been attempted through capping with protective thick oxide layers (19–21). However, these approaches inherently limit device design and process flexibility and prevent high-yield integrated electronics.

Transition-metal oxides (TMOs), for example, MoO$_3$, V$_2$O$_5$, WO$_3$, and ReO$_3$, have attracted considerable interest in charge-exchange complexes because of their large electron affinity. TMOs are most attractive candidates for STD of 2D materials (22–25) and complexes such as diamond:H (26–29). Thermal evaporation of TMO (MoO$_3$ and WO$_3$) surface acceptor on diamond:H has yielded a record sheet carrier concentration (2.52×10^{14} cm^{-2}) (27, 29) with high thermal stability (up to 450°C for ReO$_3$) (29). However, the electrical properties of TMO have been found to be vulnerable to the fabrication process of field-effect transistors (FETs) mostly due to oxide's stoichiometry degradation (30). For example, from the original diamond:H/MoO$_3$ STD layered structure to the corresponding diamond:H/MoO$_3$ FET, the carrier concentration (31) shrunk by about two orders of magnitude, from 2×10^{14} cm^{-2} to 4×10^{12} cm^{-2}, and the carrier mobility also decreased from 50 to 30 cm^2/V·s (16). Therefore, stability, efficiency, and robustness of surface acceptors in STD remain of paramount strategic value for unlocking the potential of diamond-based 2D microelectronic devices, as well as similar related semiconductors.

Here, we develop a novel approach for synthesizing a smooth, uniform, and ultrastable TMO surface acceptor thin layer with tunable electronic properties, allowing a superior 2D electrostatic match at the diamond:H/TMO interface for enhancing FET performance. The proposed concept here aims to take advantage of the tunability of TMO's electronic structure (in particular, the work function) by in situ incorporation of hydrogen bonds during atomic layer deposition (ALD). Under optimized conditions, this hydrogenated TMO (H$_y$TMO) surface acceptor shows a high robustness to a typical harsh transistor fabrication process and offers desirable electronic energy level alignment with the 2DHG channel. Our study monitors the change in surface properties of the H$_y$TMO and a nonhydrogenated reference TMO under various conditions typical of transistor fabrication. We also study the change in the electronic transfer efficiency at the diamond:H/TMO and diamond:H/H$_y$TMO interfaces before and after FET fabrication.

Our film preparation is made through ALD. First, we have adapted the process to preserve the hydrogen termination at the diamond surface.

[1]Microsystems Technology Laboratories, Massachusetts Institute of Technology, Cambridge, MA 02139, USA. [2]Research School of Chemistry, The Australian National University, Canberra, Australian Capital Territory 2601, Australia. [3]Solid State Institute and Physics Department, Technion-Israel Institute of Technology, Haifa 32000, Israel.
*These authors contributed equally to this work.
†Corresponding author. Email: tordjman@mit.edu (M.T.); alamo@mit.edu (J.A.d.A.)

Second, a novel in situ stoichiometry-modified/hydrogenated TMO surface acceptor (in our case, MoO_3) was deposited by ALD using a hydrogen source. This replaces former high-cost growth methods (32–34), including catalysis assistance using noble metals such as Pt and Pd (35–38) or irradiation under KrF laser (39). H_yMoO_{3-x} synthesized this way exhibits superior surface smoothness and homogeneity quality, shows robust stoichiometry during extreme annealing conditions, and has energy gap states that allow excellent matching electronic structure to the subsurface diamond 2DHG. The resulting diamond:H/H_yMoO_{3-x} interface structured system is found to demonstrate outstanding transistor output characteristics, reduced access resistance, and enhanced 2D hole interfacial transport.

RESULTS

Structure and stability of MoO_3 versus H_yMoO_{3-x}

Ordinarily, electronic properties of TMOs are highly sensitive to defects, such as oxygen deficiency. This translates into work function degradation and instability of their electrical properties. For instance, MoO_3 with predominant Mo^{6+} oxidation state has a high work function ($\phi = 6.8$ eV), enabling a highly efficient 2DHG at the subsurface diamond:H/MoO_3. However, this material is susceptible to oxygen loss, thus decreasing its work function upon exposure to ambient conditions (5.4 eV) (17) or, worse, during device fabrication (4.4 eV) (18). Furthermore, the application of a metal contact (that is, Ti/Au) is known to cause molybdenum cation reduction several nanometers away from the metal/MoO_3 interface. Consequently, the work function of MoO_3 and its electronic band structure exhibit a dependence on its proximity to the highly reactive metal contact (19).

In contrast, hydrogen incorporation in MoO_3 is known to increase the lattice stability and to allow tuning of the MoO_3 electronic structure by introducing a large density of gap states near the Fermi level. At the same time, it prevents the formation of alternative gap states related to oxygen reduction that pin the Fermi level at a position further up with respect to the vacuum level, and in this way helps to maintain a high work function value (5.9 eV) (20). As a consequence, hydrogenated MoO_3 (H_yMoO_{3-x}) shows a favorable energy level alignment with diamond:H, thus resulting in enhanced 2D hole transport at its interface (20).

In this report's approach, for the first time, we experimentally demonstrate a general, facile, and controllable ALD growth of MoO_3 adapted for diamond:H-terminated surfaces, which is further modified into H_yMoO_{3-x} by using hydrogen-based precursors (Fig. 1, left side). The schematic diagram of the working principles of diamond:H STD with MoO_3 and H_yMoO_{3-x} is represented in Fig. 1 (right side). This shows the cross-section interface of MoO_3 and H_yMoO_{3-x} STD layers on diamond:H transistors and their corresponding energy band structures (20).

The band structure of MoO_3 differs in its three oxidation states—Mo^{6+}, Mo^{5+}, and Mo^{4+}—following their respective degrees of oxygen reduction. Oxygen reduction induces vacancies that lead to the appearance of bonding and anti-bonding d-d and d-d* bands in the bandgap, thus upshifting the Fermi level and reducing the work function (Fig. 1, upper set of diagrams). In contrast, for the case of H_yMoO_3, the introduction of hydrogen atoms forms strong covalent bonds with the bridging and terminal oxygen atoms of Mo–O bonds (see atomistic schematic representation of O–H bonds in red-green in Fig. 1, lower left). The O–H covalent bonds yield intervalence π* electron states with energies close to the conduction band edge (20). In addition, oxygen

reduction from perfect H_yMoO_3 stoichiometry into H_yMoO_{3-x} (Fig. 1, lower) is mitigated, thus preventing the appearance of further oxygen vacancy d-d* states (as in Mo^{4+}). As a result, no significant shift of the Fermi level is expected, thus preserving the high work function of the material.

MoO_3 and H_yMoO_{3-x} ALD synthesis and properties

Existing ALD processes for MoO_3 (40) are traditionally assisted by oxygen plasma and cannot be used in our present case as it degrades the C–H terminating bonds at the diamond:H surface—a crucial condition for surface doping. Other ALD recipes (41, 42) using oxygen-based precursors (that is, O_3) as first iterative pulses were also found to affect somehow the diamond:H surface (Fig. 1A). Here, a different approach was used. We first pre-anneal vacuum chamber up to 350°C to desorb atmosphere-related adsorbates from the diamond:H surface. We then initialize the ALD process with a Mo-based precursor pulse [that is, $Mo(CO)_6$] followed by the complementary oxygen source precursor pulse (that is, O_3). The vacuum chamber is purged and pumped after each cycle, allowing the preservation of the diamond:H surface as intact as possible (Fig. 1, B and C). Noteworthy are our first MoO_3 ALD process trials in which we started with O_3 pulses followed by $Mo(CO)_6$ ones. This resulted in a poor surface conductivity, most likely due to the pressurized O species pulses damaging the diamond:H surface termination [see (43)].

The STD layer of MoO_3 was deposited by ALD using $Mo(CO)_6$ and O_3 as precursors. For H_yMoO_{3-x}, the precursors were $C_{12}H_{30}MoN_4$ and H_2O. H_2O constitutes the hydrogenation source for H_yMoO_{3-x}. Different flux ratios of the precursors were studied. The detailed ALD growth conditions are described in the Supplementary Materials. The final ALD-grown MoO_3 and H_yMoO_{3-x} films, with thickness of ~4 nm, exhibit a uniform surface, as seen by atomic force microscopy (AFM). A 3D plane AFM characterization of the obtained diamond:H/H_yMoO_{3-x} is shown in Fig. 2D, indicating a surface average roughness (R_a) of 0.29 nm along an area of 1 μm × 1 μm. A R_a of 0.64 nm is obtained along an area of 10 μm × 10 μm, as shown in fig. S1. Similar results have been obtained for diamond:H/MoO_3. In addition, fig. S1 (A and B) shows the top view and z-direction profile versus distance along the x axis of the corresponding AFM surfaces, and fig. S1 (D and E) gives nanoscale topography resolutions. X-ray diffraction (XRD) measurements of the as-grown MoO_3 and H_yMoO_{3-x} reveal peaks mostly related to the monoclinic β-MoO_3 crystalline phase. They increase in number and intensity following process treatments (see fig. S2 and related comments in the Supplementary Materials).

The stoichiometry of the as-deposited ALD MoO_3 and H_yMoO_{3-x} films was evaluated by measuring the Mo 3d and O 1s core-level spectra by x-ray photoelectron spectroscopy (XPS). Each core-level spectrum was deconvolved as presented in Fig. 2A for Mo 3d and Fig. 2B for O 1s. The XPS Mo 3d results indicate the coexistence of Mo^{6+}, Mo^{5+}, and Mo^{4+} oxidation states, where Mo^{6+} have a $3d_{5/2}$ and $3d_{3/2}$ spin-orbit doublet peaks at a binding energy (BE) of 232.4 eV (with a splitting BE of 3.2 eV), Mo^{5+} doublet peaks at 231.6 eV, and Mo^{4+} peaks at 229.1 eV. On the other hand, for the O 1s in Fig. 2B, the two deconvolved subpeaks appear at 530.3 and 531.6 eV, respectively, and are attributed to Mo–O and Mo–OH bonding (20).

To correlate the H_yMoO_{3-x} film stoichiometric chemistry with the ALD growth conditions, we presented the percentage of the various Mo oxidation states (Mo^{6+}, Mo^{5+}, and Mo^{4+}; filled symbols) and O states (Mo–O and Mo–OH; empty symbols) versus the different flux ratio of the $C_{12}H_{30}MoN_4$ to H_2O precursors during the various ALD growths in Fig. 2C.
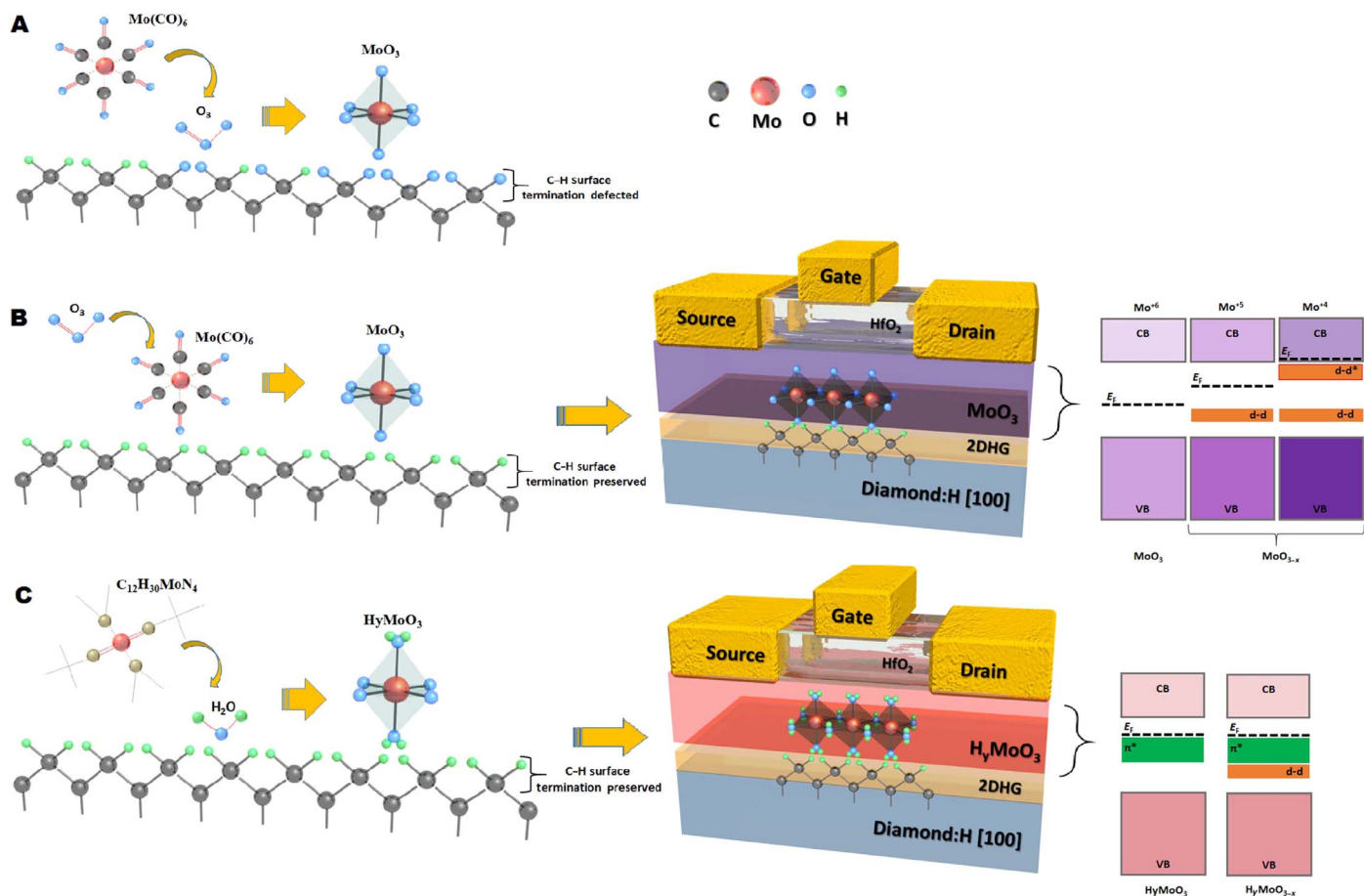
Fig. 1. Schematic structure of diamond:H surface undergoing different ALD processes and their resulting interface electronic properties with diamond:H/MoO$_3$ versus diamond:H/H$_y$MoO$_{3-x}$ transistors. (**A**) Application of a typical MoO$_3$ ALD process on diamond:H, resulting in surface termination degradation. (**B** and **C**) Modified ALD process of MoO$_3$ and H$_y$MoO$_{3-x}$ for preserving diamond:H termination. Right side from top to bottom: Schematic cross-sectional diagram with interface atomistic representations of diamond:H/MoO$_3$ (top) and diamond:H/H$_y$MoO$_{3-x}$ (bottom) FETs and their respective electronic band energy structures with different oxidation state ratios. CB, conduction band; VB, valence band.

Two interesting results are worth noting here. First, there is a positive correlation in the percentage/concentration of Mo^{6+} oxidation state and Mo–OH bond (Fig. 2C). This suggests that the involved precursors encourage a nucleation of the compound OH–Mo–O, that is, H$_y$MoO$_{3-x}$, with the Mo^{6+} state, which represents the highest molybdenum oxidation state. Second, at a flux ratio of C$_{12}$H$_{30}$MoN$_4$ to H$_2$O of 6.2, we obtain the highest concentration of the Mo^{6+} oxidation state in the H$_y$MoO$_{3-x}$ film. Thus, we selected this sample for further analysis and for FET fabrication. On the basis of the percentage contents of oxidation states Mo^{6+}, Mo^{5+}, and Mo^{4+} from the Mo 3d core levels and bonds Mo–O and Mo–OH from O 1s, we obtain a composition H$_{2.3}$MoO$_{2.5}$ for this sample. This compound is rich in Mo–OH compounds (~78%) and has a low oxygen vacancy rate (~18%). Note here that the main mechanism responsible for the Mo–OH formation in H$_y$MoO$_{3-x}$ is associated with the fact that hydrogen atoms from the H$_2$O precursor form covalent bonds with the terminal oxygen and bridging atoms of MoO$_x$ (see atomic sketch in Fig. 1) (*21*, *22*). The coexistence of a low fraction of Mo^{5+} and Mo^{4+} reduction states further supports the oxide reduction characteristics of hydrogen-incorporated MoO$_3$, forming the final H$_y$MoO$_{3-x}$ (*20*).

Amelioration of hole transfer at the TMO/2DHG interface

To study the stoichiometry tunability and thermal stability of the ALD-grown MoO$_3$ and H$_y$MoO$_{3-x}$ films, we investigated the impact of rapid thermal annealing (RTA) on the films. Before RTA and to facilitate electrical Hall effect characterization, we deposited Ti/Au ohmic contacts of a van der Pauw structure through a shadow mask for a minimal intervention process fabrication. Following this, RTA at 600°C in N$_2$ ambient was sequentially performed for several minutes. After each RTA treatment, the diamond:H/MoO$_3$ electrical properties were measured by Hall effect to monitor the evolution of the carrier concentration and mobility.

The results shown in Fig. 3 (A and B) depict a strong degradation of the 2D hole concentration and mobility for the MoO$_3$ sample. Specifically, after an RTA treatment for 3 min, the 2D hole concentration severely deteriorated from 7.9×10^{13} cm^{-2} to 5.3×10^{12} cm^{-2}, and the hole mobility dropped from 26.2 to 18.4 cm^2/V·s. These results are most likely due to the fragile nature of MoO$_3$ and its oxidation state reduction upon RTA. This is confirmed by corresponding Mo 3d spectra analysis of XPS measurements (shown in Fig. 3C). The fresh diamond:H/MoO$_3$ sample before RTA exhibits a high Mo^{6+} (94%) content. After 5-min
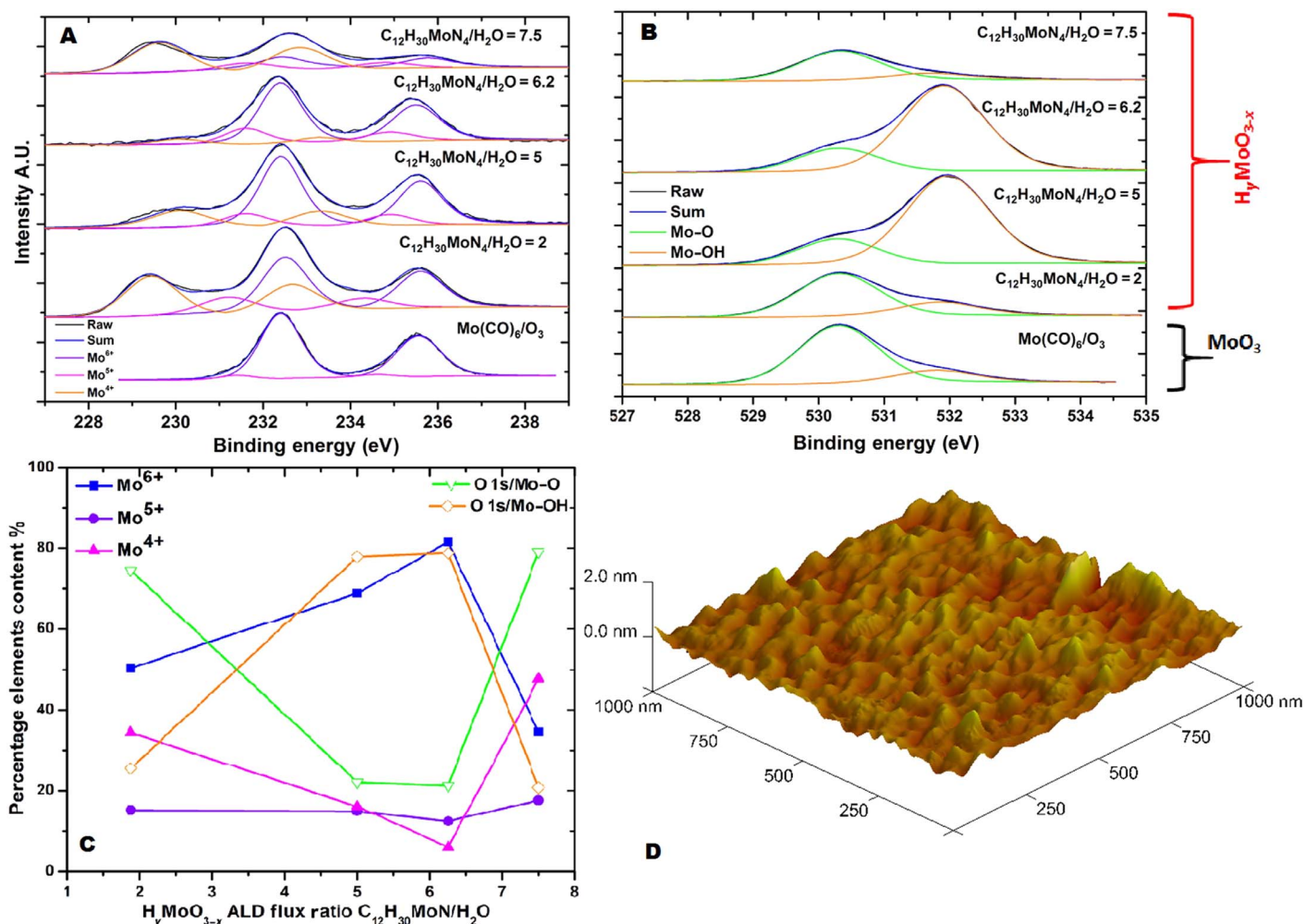
Fig. 2. XPS of ALD-grown MoO₃ and HᵧMoO₃₋ₓ films. (**A**) Deconvolution of Mo 3d core-level spectra of Mo oxidation states Mo⁶⁺, Mo⁵⁺, and Mo⁴⁺ for MoO₃ and HᵧMoO₃₋ₓ ALD grown with different precursor ratios. (**B**) Deconvolution of O 1s core-level spectra of O states Mo–O and Mo–OH for MoO₃ and HᵧMoO₃₋ₓ ALD grown with different precursor ratios. (**C**) Dependence of Mo 3d oxidation states and O 1s states for Mo–O and Mo–OH percentages on the flux ratio of C₁₂H₃₀MoN₄ to H₂O. (**D**) AFM 3D view of 1 μm × 1 μm area of diamond:H/HᵧMoO₃₋ₓ (the input flux ratio of C₁₂H₃₀MoN₄ to H₂O is 6.2 for AFM sample). A.U., arbitrary units.

RTA, there is a high oxygen deficiency rate with a decrease in Mo⁶⁺ content (57%), increase in Mo⁵⁺ (from 6 to 34%), and an appearance of Mo⁴⁺ (from 0 to 9%) oxide states (Fig. 3C).

In stark contrast, for the case of $H_{2.3}MoO_{2.5}$ ALD, the application of the same RTA conditions enhances the hole concentration and mobility in a significant manner. The as-deposited diamond:H/$H_{2.3}MoO_{2.5}$ sample shows weak p-type characteristics with a sheet hole concentration of 3.3×10^{12} cm^{-2} and a hole mobility of 9.8 cm²/V·s (Fig. 3, A and B). After RTA at 600°C, both the hole concentration and mobility increased with annealing time and reached the highest values after 3-min RTA: 1.9×10^{13} cm^{-2} and 22.4 cm²/V·s, respectively. We attribute this to an improvement in the carrier transfer efficiency and quality of the diamond:H/$H_{2.3}MoO_{2.5}$ interface after thermal annealing. Longer RTA than 5 min degrades the characteristics, perhaps as a result of out-diffusion of hydrogen from diamond:H and/or damaging the $H_{2.3}MoO_{2.5}$ smooth morphology.

The respective Mo 3d spectral measurements reveal a much lower oxidation reduction rate for HᵧMoO₃₋ₓ as compared to MoO₃ after RTA exposure. We observe a small decrease in Mo⁶⁺ (from 82 to 76%)

content, a modest increase in Mo⁵⁺ (from 12 to 20%), and a small reduction in Mo⁴⁺ (from 6 to 4%) oxide states (Fig. 3C).

In addition, ultraviolet photoemission (UPS) measurements with a HeI (21.22 eV) excitation line were carried out on the TMO layer reference samples right after their synthesis and following their respective FET process fabrication conditions. In MoO₃ and MoO₃₋ₓ, indicating the as-grown layer and the same layer following process fabrication, respectively, UPS reveals work function values of 6.7 and 5.05 eV (Fig. 3F). MoO₃ eventually shows the appearance of occupied states at 2.2-eV BE near the Fermi level inside the bandgap (Fig. 3D) corresponding to the d-d bands, presumably formed by oxygen reduction in the layer (44). In HᵧMoO₃ and HᵧMoO₃₋ₓ, indicating the as-grown hydrogenated layer and the same layer after the complete device process (including RTA), respectively, UPS reveals a consistent work function value of 5.9 eV for both of them (Fig. 3F) and shows the additional appearance of the π* bandgap states at 1.2-eV BE away from the Fermi level (Fig. 3D). This is in agreement with a previous report (45). Note that the HᵧMoO₃₋ₓ layer (Fig. 3D, red line) after full FET process fabrication is the only one having both types of gap states, d-d and π*
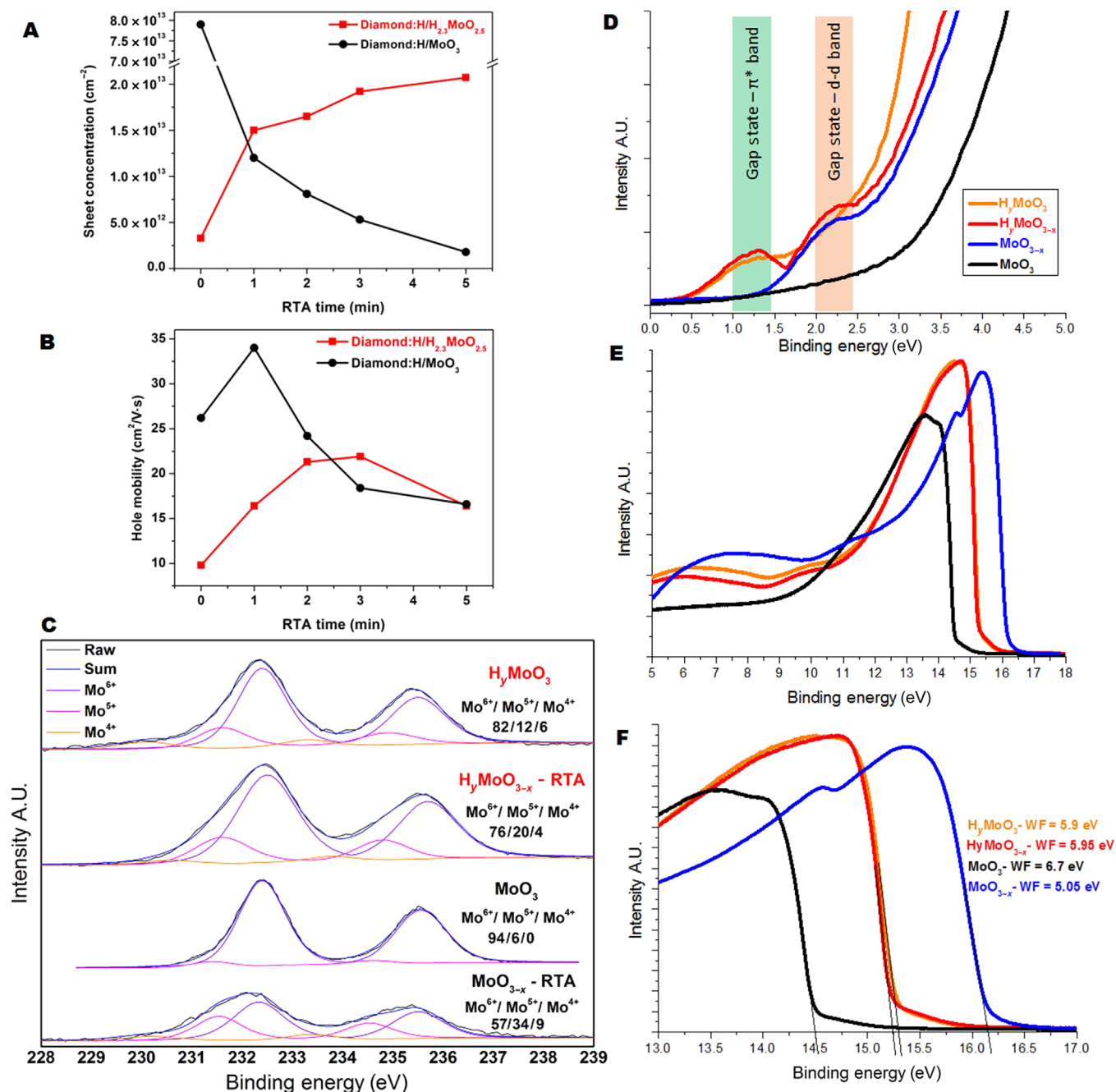
Fig. 3. Electrical and surface characterizations before and after process fabrication. (**A**) Hall effect sheet concentration and (**B**) hole mobility of diamond:H/$H_{2.3}MoO_{2.5}$ versus diamond:H/MoO_3 STD structures versus RTA effect (600°C). (**C**) XPS Mo 3d core-level spectra measurements of diamond:H/$H_{2.3}MoO_{2.5}$ and diamond:H/MoO_3 before and after 6-min RTA. Mo oxidation state ratios of Mo^{6+}, Mo^{5+}, and Mo^{4+} are noted. UPS spectra of the Mo oxide synthesized layers showing (**D**) near Fermi edge region valence band and (**E** and **F**) secondary cutoff region, right after their synthesis (MoO_3 and H_yMoO_3), and following their respective optimized process fabrication conditions (MoO_{3-x} and H_yMoO_{3-x}).

bands close to the Fermi edge, whereas H_yMoO_3 (Fig. 3D, orange line) and MoO_{3-x} (Fig. 3D, blue line) have only either the π* or d-d bands, respectively.

Improved 2D hole transport in diamond:H/$H_{2.3}MoO_{2.5}$ FETs
Diamond:H/$H_{2.3}MoO_{2.5}$ and diamond:H/MoO_3 FETs were fabricated with the processing detailed in fig. S3 and with a typical cross-section

interface structure conformity as indicated in fig. S4. The RTA step (3 min at 600°C in N_2 environment) was omitted for the diamond:H/MoO_3 device fabrication because it was found to degrade the interfacial characteristics. All other process steps were identical for both types of FETs and were performed at the same time.

Electrical characteristics of typical FETs with identical dimensions (see caption) are shown in Fig. 4. Both devices show p-type behavior,

but the diamond:H/H$_{2.3}$MoO$_{2.5}$ FETs are vastly superior to the diamond:H/MoO$_3$ devices. The diamond:H/H$_{2.3}$MoO$_{2.5}$ FETs exhibit well-saturated output characteristics with an ON/OFF ratio of five orders of magnitude. In contrast, the diamond:H/MoO$_3$ FETs show much lower current, higher output conductance, and very poor subthreshold behavior. This could be due to deterioration of the diamond:H/MoO$_3$ interface during processing and, consequently, to a nonfavorable energy level alignment formation at the diamond:H/MoO$_{3-x}$ interface caused by gap states from oxygen reduction.

Key metrics of the two types of transistors are summarized in Fig. 5B. This also includes measurement on Hall bar structures that, as detailed above, were fabricated separately through a benign fabrication process.
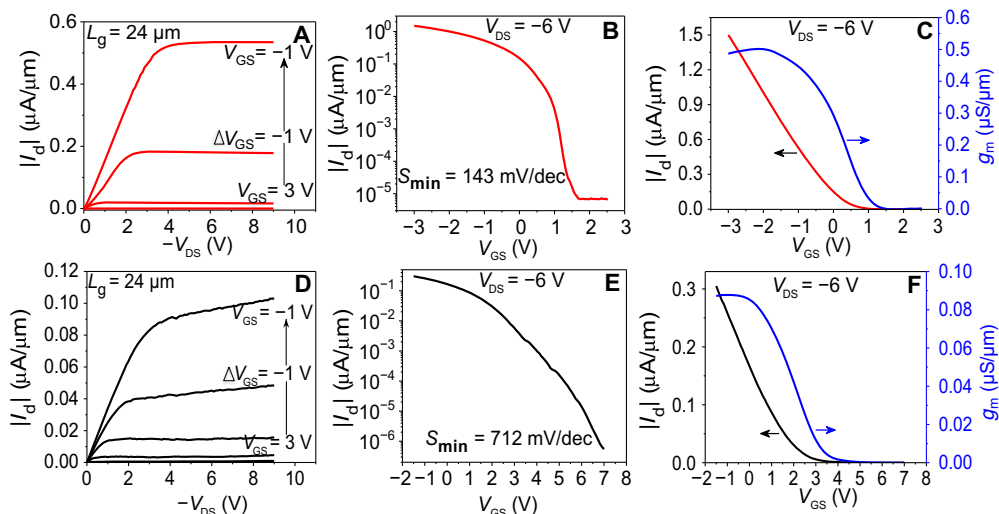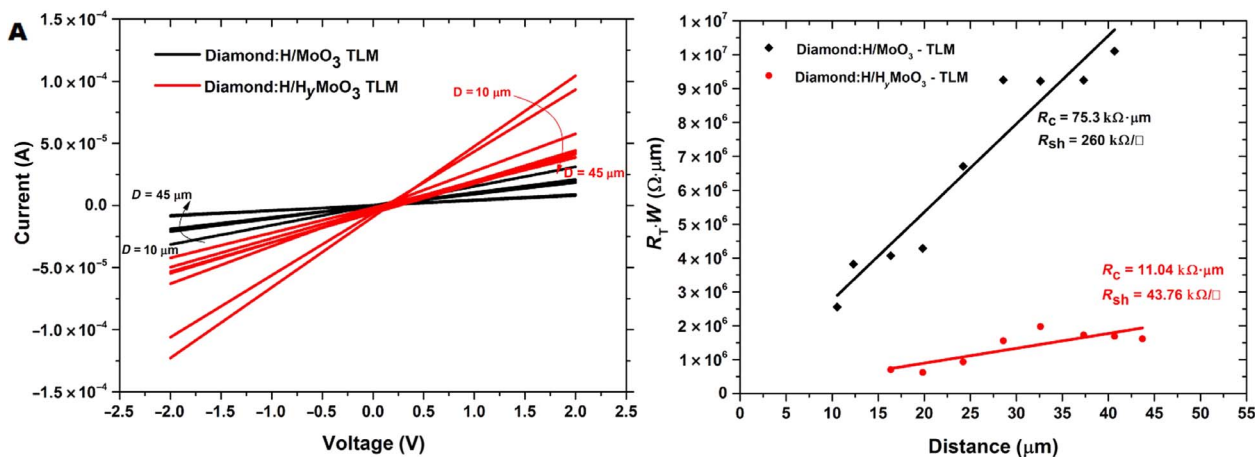

Fig. 4. Comparison of FET characteristics. Comparison of diamond:H/H$_{2.3}$MoO$_{2.5}$ (**A** to **C**) and diamond:H/MoO$_3$ (**D** to **F**) FET characteristics with the same dimensions: 24-μm gate length, 40-μm gate width, and 15-μm source/drain-to-gate separation: (A versus D) output characteristics, (B versus E) subthreshold characteristics, and (C versus F) transconductance and transfer characteristics (note the different scales).

Fig. 5. Transmission line model and key metric values for both transistors. (**A**) Left: *I-V* curves as measured from TLM test structures with distances (*D* = 10 to 45 μm) on diamond:H/MoO$_3$ (black lines) and diamond:H/H$_y$MoO$_{3-x}$ (red lines) samples (right). Linear fitting curves of corresponding sample TLM pattern. *R*$_c$ and *R*$_{sh}$ stand for contact and sheet resistance, respectively. The test structures are integrated with the FETs and have undergone the entire FET fabrication process. Distance values are actual measurements obtained from scanning electron microscopy (SEM). (**B**) Comparison of key figures of merit in diamond:H/MoO$_3$ and diamond:H/H$_{2.3}$MoO$_{2.5}$ FET devices after full process fabrication and Hall bar structures before process fabrication.

The Hall measurements yield a hole mobility and sheet concentration of 22.4 $cm^2/V \cdot s$ and 1.9×10^{13} cm^{-2} for diamond:H/$H_{2.3}MoO_{2.5}$ (following 3-min RTA) compared to 26.2 $cm^2/V \cdot s$ and 7.9×10^{13} cm^{-2} for diamond:H/MoO_3 (without RTA). The contrast between the electrical characteristics of the FETs and the Hall structures could not be more stark. The FET fabrication process results in severe degradation of the diamond:H/MoO_3 structures with respect to the diamond:H/H_yMoO_{3-x} ones.

Classic two-port transmission line model (TLM) measurements were carried out on the diamond:H/H_yMoO_{3-x} and diamond:H/MoO_3 samples following device process fabrication (Fig. 5). The results show a sevenfold lower contact resistance value (R_c = 11 kΩ μm) with a significant lower sheet resistance value (R_{sh} = 43 kΩ/sq) for diamond:H/H_yMoO_{3-x} compared to diamond:H/MoO_3 (R_c = 75 kΩ μm and R_{sh} = 260 kΩ/sq). These results further illustrate the superior resilience of the diamond:H/H_yMoO_{3-x} structures to the FET fabrication process.

Superiority of diamond:H/H_yMoO_{3-x} interface modulation

The previous section has shown a significantly improved robustness of the diamond:H/H_yMoO_{3-x} interface with respect to the diamond:H/MoO_3 interface in the course of FET fabrication. In this section, we discuss the role of interface modulation of the resulting 2DHG and TMO's band energy co-alignment in these results.

The initial case of unprocessed Hall bar diamond:H/MoO_3 structure (Fig. 6A) shows a high-volume hole gas accumulation layer (7.9×10^{13} cm^{-2}) with a hole mobility of 26.2 $cm^2/V \cdot s$. These results are attributed to the MoO_3 high work function value of ~6.7 eV, which yields a deep-lying 2DHG with a high carrier concentration. However, this scenario is unfortunately not preserved after FET fabrication because MoO_3 tends to rapidly reduce to MoO_{3-x} during the process (Fig. 3C). The diamond:H/MoO_{3-x} structure after FET fabrication (Fig. 6B) suffers from a reduced volume hole gas accumulation layer (3.2×10^{12} cm^{-2}) with a poor hole mobility (2.1 $cm^2/V \cdot s$) due to a degraded work function value of ~5 eV. Consequently, a smaller density of carriers is available for transport in the 2DHG. The reduced MoO_{3-x} gives rise to separated d-d and d-d* gap states (Fig. 3D) that can accommodate electrons and contribute to form a 2DHG on the diamond side of the interface. In the case of MoO_3, electrons are most likely transferred into the conduction band.

In contrast to this, the diamond:H/H_yMoO_{3-x} interface FET (Fig. 6C) benefits from a relatively high density hole gas accumulation layer (5.1×10^{12} cm^{-2}) and a relatively high hole mobility of 19.5 $cm^2/V \cdot s$ because of the H_yMoO_{3-x} robust work function value of 5.9 eV. In this case, the purposefully modulated $H_{2.3}MoO_{2.5}$ stoichiometry layer (tuned by selecting the optimized RTA conditions that yield maximum carrier concentration) benefits from a favorable direct transport pathway for available carriers from the 2DHG channel via its aligned and joined together d-d and π-π* gap states (oxidation states as observed in Fig. 3, C and D) along the layer to the contacts. This later advantage is also supported by the significantly lower access resistance results for this FET device compared to the previous case (Fig. 5B).

The thus obtained modulated diamond:H/H_yMoO_{3-x} interface demonstrates three simultaneous advantages: (i) a superior endurance of the H_yMoO_{3-x} layer properties during FET fabrication that enhances its chemical stability and keeps the high work function value of H_yMoO_{3-x} during device process fabrication; (ii) a preserved deep-lying 2DHG at the diamond subsurface, generating a relatively high carrier density and mobility; and (iii) an aligned electronic structure of the tuned diamond:H/$H_{2.3}MoO_{2.5}$ interface, giving rise to intermediate
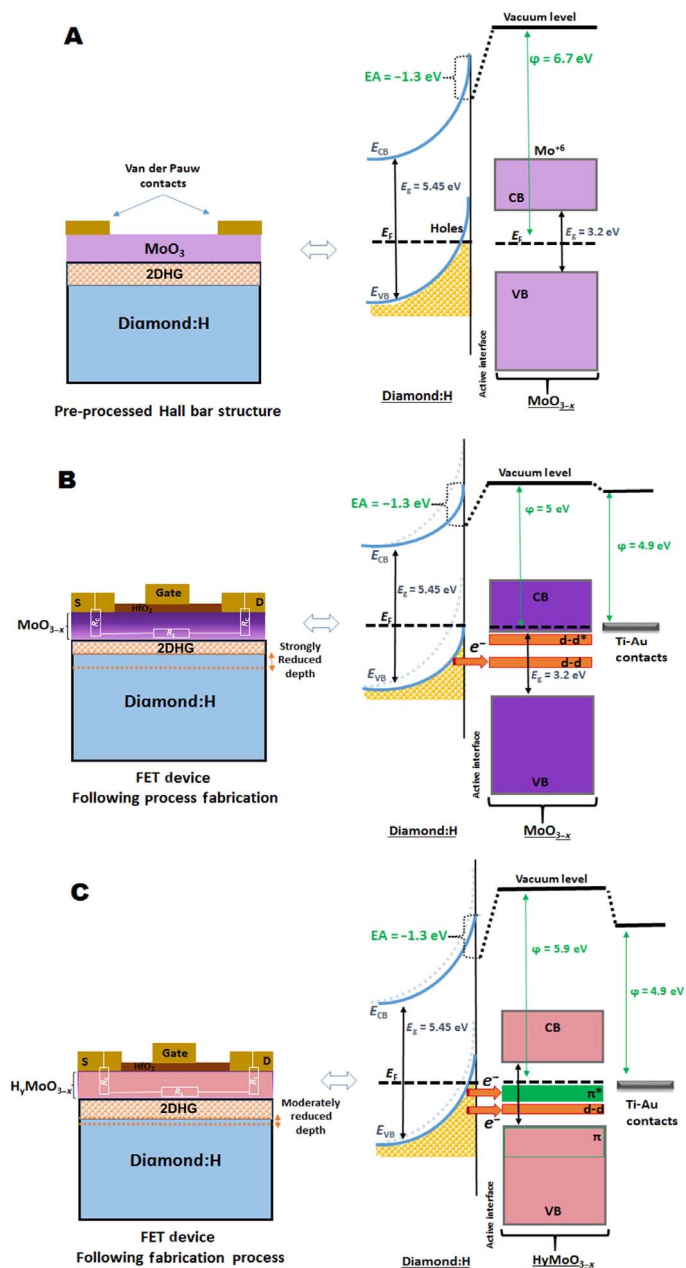

Fig. 6. Band energy diagram comparison of the different cross-section heterostructure cases. Band energy diagram of the cross-section heterostructure for the different interface configurations following their stoichiometric situation: (**A**) diamond:H/MoO_3 pre-processed structure, (**B**) diamond:H/MoO_{3-x}/Ti-Au, and (**C**) diamond:H/H_yMoO_{3-x}/Ti-Au after device process fabrication.

d-d and π-π* gap states positioned in the bandgap, making it most favorable for carrier transport from the diamond 2DHG to the contacts.

DISCUSSION

A facile general strategy for integrating and modulating synergically the electrical structures of TMO as a surface acceptor layer used in STD of diamond is proposed and demonstrated. We use hydrogen incorporation in MoO_3 to obtain a modulated H_yMoO_{3-x} following optimized RTA as an STD layer in diamond:H–based FETs. We find

that, in contrast to conventional ALD-deposited MoO_3, the novel controllable ALD-grown H_yTMO approach showed (i) improved surface acceptor morphology smoothness; (ii) immunity to harsh processing FET fabrication conditions, which have been shown to be detrimental for all TMO surface acceptors reported so far and specifically to MoO_3; and (iii) improved hole transfer across the diamond:H/H_yMoO_{3-x} interface because of a favorable band energy alignment formed after modulation.

The novel tunable H_yTMO (diamond:H/H_yMoO_{3-x}) surface acceptor is further validated by demonstrating significant improved FET characteristics compared to the conventional TMO (diamond:H/MoO_{3-x}) case. This solution demonstrates the feasibility of sustaining the surface acceptor materials' structural performance in the course of device fabrication and promises a general strategy to realize improved functional surface charge acceptors for 2D extreme semiconductors, such as diamond. This novel approach applicability should expand to other fields where TMOs are playing an increasing role such as optoelectronics, photonics, photovoltaics, photocatalysis, and sensing.

MATERIALS AND METHODS

Samples preparation

Undoped type IIa (100) diamond single-crystal samples were cleaned in boiling piranha solution (mixture of concentrated H_2SO_4 and 30% H_2O_2) and then exposed to pure hydrogen plasma in a chemical vapor deposition reactor at a temperature of about 650°C for 40 min to prepare a hydrogen-terminated surface. When exposed to ambient air, hydrogen-terminated diamond, that is, diamond:H, easily absorbs aqueous species, which work as spontaneous surface electron acceptors. The resulting diamond:H/H_2O conductive surface shows a sheet hole concentration of 1.8×10^{13} cm^{-2} and a hole mobility of 20.6 cm^2/V·s at room temperature.

The diamond:H/H_2O samples were then in situ annealed in the ALD vacuum chamber (10^{-6} torr) at 350°C for several minutes to desorb any air-related adsorbates and to exclude their eventual contribution to conductivity. Following this, MoO_3 was deposited by ALD at 167°C using sequential pulses of molybdenum hexacarbonyl [Mo(CO)$_6$] and ozone (O$_3$) precursors and purging pump for each cycle. The optimized thickness was 4 nm and was verified by ellipsometry. In a separate diamond:H sample, ~4-nm-thick H_yMoO_{3-x} ALD was deposited using bis(t-butylimido) bis(dimethylamino) molybdenum (VI) ($C_{12}H_{30}MoN_4$) as Mo precursor and pure H_2O as O and OH source at 350°C. The ALD growth conditions were optimized by examining different precursor flux ratios.

Characterization

Electrical measurements consisting of carrier type, carrier concentration, and mobility were measured using Hall effect in a van der Pauw configuration with a magnetic field up to 1.5 T. Four symmetric Ti/Au electrodes placed on the top layer of the samples were used as electrical contacts.

XPS measurements were used to characterize the chemical bonding and to determine the band structure of the films. These measurements were conducted in a Thermo VG Scientific Sigma Probe system using a monochromatic Al Kα (1486.6 eV) x-ray source in bulk and surface modes. Mo 3d and O 1s core-level spectra were collected with a pass energy of 20 eV. The spectrometer BE was calibrated by setting the $4f_{7/2}$ core level of Au to 84.0 eV. Curve fitting was done by the

XPSPEAK 4.1 software using Voigt function convolution with a Shirley-type background subtraction. HeI (hv = 21.22 eV) ultraviolet light was used for UPS. The samples were biased at −5 V in UPS measurements to separate the high BE cutoff regions and retrieve the absolute estimation of work function values. XRD data (fig. S2) were obtained using a Bruker D8 ADVANCE Eco XRD with Cu Kα radiation (α = 1.5406 Å) from 5° to 65° at a step of 0.02° and a count time of 0.2 s.

FET fabrication

Diamond:H-based FETs were fabricated following the process outlined in fig. S2. Briefly, after H_yMoO_{3-x} and MoO_3 ALD, 20-nm Ti/200-nm Au source-drain electrodes were electron-beam–evaporated through a shadow mask. Then, 3-min RTA at 600°C in a nitrogen environment was performed only for the diamond:H/$H_{2.3}MoO_{2.5}$ sample, followed by the deposition of 20-nm HfO_2 by ALD at 250°C as the dielectric layer. Finally, the channel isolation using electron-beam lithography and reactive-ion etching and the subsequent 20-nm Ti/200-nm Au gate deposition through a shadow mask were performed to produce the final FETs.

Two-port transmission line measurements

Classic two-port TLM measurements were carried out on the diamond:H/H_yMoO_{3-x} and diamond:H/MoO_3 samples following device fabrication. Linear fits of total resistance (R_T) versus TLM pattern distance (L) of 10 to 40 μm following $R_T = 2R_c + LR_{sh}/W$ were then performed. The channel width (W) was 40 μm, R_c is the contact resistance, and R_{sh} is the semiconductor sheet resistance.

Hole mobility

The 2D hole mobility (μ) for diamond:H/$H_{2.3}MoO_{2.5}$ and diamond:H/MoO_3 FETs is evaluated on the basis of the measured transfer characteristics in the linear regime by performing the calculation with the formula (46)

$$\mu = \frac{L_g}{W \times (\varepsilon_o \varepsilon_\tau/d) \times V_{DSi}} \times \frac{dI_D}{dV_{GSi}} \qquad (1)$$

where the channel length L_g is 24 μm and the channel width W is 40 μm for both kinds of FETs. The permittivity ε_o in air is 8.85×10^{-12} F/m, the dielectric constant ε_r for HfO_2 is 18 (41), and the thickness d is 20 nm.

In the derivation of mobility, we used the intrinsic values of V_{GS}, that is, V_{GSi}, and intrinsic values of V_{DS}, that is, V_{DSi}, obtained after accounting for the role of the source and drain resistances (46). Finally, after calculation, the maximum mobility from diamond:H/$H_{2.3}MoO_{2.5}$ and diamond:H/MoO_3 is 19.5 and 2.1 cm^2/V·s, respectively, as presented in Fig. 5B.

Sheet hole concentration

The sheet hole concentration (P_s) is evaluated from (46)

$$P_S = \frac{(\varepsilon_o \varepsilon_\tau/d) \times (V_{GSi} - V_T)}{e} \qquad (2)$$

where V_{GSi} is the intrinsic gate voltage, V_T is the threshold voltage extracted from the transfer characteristics, and e is the elementary charge. This calculation yields a sheet hole concentration of 5.1×10^{12} cm^{-2} and 3.2×10^{12} cm^{-2}, respectively, for diamond:H/$H_{2.3}MoO_{2.5}$ and diamond:H/MoO_3, as presented in Fig. 5B.

SUPPLEMENTARY MATERIALS

Supplementary material for this article is available at http://advances.sciencemag.org/cgi/content/full/4/9/eaau0480/DC1

Surface characterization
FET fabrication
FET interface structure
Fig. S1. AFM characterization on 10 μm × 10 μm areal top surface of diamond:H/H$_{2.3}$MoO$_{2.5}$.
Fig. S2. XRD pattern obtained for the ALD thin film on diamond:H substrate.
Fig. S3. Fabrication procedure of diamond:H/H$_y$MoO$_{3-x}$ MOSFET.
Fig. S4. Cross-section SEM of a diamond:H/H$_y$MoO$_3$ (10 nm)/Ti-Au (10 to 100 nm) prepared sample.

REFERENCES AND NOTES

1. J. Ristein, Surface transfer doping of semiconductors. *Science* **313**, 1057–1058 (2006).
2. P. Strobel, M. Riedel, J. Ristein, L. Ley, Surface transfer doping of diamond. *Nature* **430**, 439–441 (2004).
3. V. Chakrapani, J. C. Angus, A. B. Anderson, S. D. Wolter, B. R. Stoner, G. U. Sumanasekera, Charge transfer equilibria between diamond and an aqueous oxygen electrochemical redox couple. *Science* **318**, 1424–1430 (2007).
4. I. E. Jacobs, A. J. Moulé, Controlling molecular doping in organic semiconductors. *Adv. Mater.* **29**, 1703063 (2017).
5. X. Zhang, Z. Shao, X. Zhang, Y. He, J. Jie, Surface charge transfer doping of low-dimensional nanostructures toward high-performance nanodevices. *Adv. Mater.* **28**, 10409–10442 (2016).
6. K. J. Rietwyk, Y. Smets, M. Bashouti, S. H. Christiansen, A. Schenk, A. Tadich, M. Edmonds, J. Ristein, L. Ley, C. I. Pakes, Charge transfer doping of silicon. *Phys. Rev. Lett.* **112**, 155502 (2014).
7. W. Chen, D. Qi, X. Gao, A. T. S. Wee, Surface transfer doping of semiconductors. *Prog. Surf. Sci.* **84**, 279–321 (2009).
8. J. Jie, W. Zhang, K. Peng, G. Yuan, C. S. Lee, S.-T. Lee, Surface-dominated transport properties of silicon nanowires. *Adv. Funct. Mater.* **18**, 3251–3257 (2008).
9. J. Ristein, Surface transfer doping of semiconductors. *Science* **313**, 1057–1058 (2006).
10. C. J. H. Wort, R. S. Balmer, Diamond as an electronic material. *Mater. Today* **11**, 22–28 (2008).
11. M. I. Landstrass, K. V. Ravi, Resistivity of chemical vapor deposited diamond films. *Appl. Phys. Lett.* **55**, 975–977 (1989).
12. O. A. Williams, R. B. Jackman, Surface conductivity on hydrogen terminated diamond. *Semicond. Sci. Technol.* **18**, S34–S40 (2003).
13. C. E. Nebel, Surface-conducting diamond. *Science* **318**, 1391–1392 (2007).
14. C. Sauerer, F. Ertl, C. E. Nebel, M. Stutzmann, P. Bergonzo, O. A. Williams, R. A. Jackman, Low temperature surface conductivity of hydrogenated diamond. *Phys. Status Solidi A* **186**, 241–247 (2001).
15. P. Strobel, J. Ristein, L. Ley, K. Seppelt, I. V. Goldt, O. Boltalina, Surface conductivity induced by fullerenes on diamond: Passivation and thermal stability. *Diam. Relat. Mater.* **15**, 720–724 (2006).
16. D. P. Langley, Y. Smets, C. B. Stark, M. T. Edmonds, A. Tadich, K. J. Rietwyk, A. Schenk, M. Wanke, Q.-H. Wu, P. J. Barnard, L. Ley, C. I. Pakes, Surface transfer doping of diamond with a molecular heterojunction. *Appl. Phys. Lett.* **100**, 032103 (2012).
17. D. Qi, W. Chen, X. Gao, L. Wang, S. Chen, K. P. Loh, A. T. S. Wee, Surface transfer doping of diamond (100) by tetrafluoro- tetracyanoquinodimethane. *J. Am. Chem. Soc.* **129**, 8084–8085 (2007).
18. A. Laikhtman, A. Lafosse, Y. Le Coat, R. Azria, A. Hoffman, Interaction of water vapor with bare and hydrogenated diamond film surfaces. *Surf. Sci.* **551**, 99–105 (2004).
19. H. Kawarada, H. Tsuboi, T. Naruo, T. Yamada, D. Xu, A. Daicho, T. Saito, A. Hiraiwa, C-H surface diamond field effect transistors for high temperature (400°C) and high voltage (500 V) operation. *Appl. Phys. Lett.* **105**, 013510 (2014).
20. C. Verona, W. Ciccognani, S. Colangeli, E. Limiti, M. Marinelli, G. Verona-Rinati, Comparative investigation of surface transfer doping of hydrogen terminated diamond by high electron affinity insulators. *J. Appl. Phys.* **120**, 025104 (2016).
21. M. Imura, R. G. Banal, M. Liao, J. Liu, T. Aizawa, A. Tanaka, H. Iwai, T. Mano, Y. Koide, Effect of off-cut angle of hydrogen-terminated diamond(111) substrate on the quality of AlN towards high-density AlN/diamond(111) interface hole channel. *J. Appl. Phys.* **121**, 025702 (2017).
22. F. Xia, Z. Shao, Y. He, R. Wang, X. Wu, T. Jiang, S. Duhm, J. Zhao, S.-T. Lee, J. Jie, Surface charge transfer doping via transition metal oxides for efficient p-type doping of II–VI nanostructures. *ACS Nano* **10**, 10283–10293 (2016).
23. D. Xiang, C. Han, J. Wu, S. Zhong, Y. Liu, J. Lin, X.-A. Zhang, W. P. Hu, B. Özyilmaz, A. H. Castro Neto, A. T. S. Wee, W. Chen, Surface transfer doping induced effective modulation on ambipolar characteristics of few-layer black phosphorus. *Nat. Commun.* **6**, 6485 (2015).
24. J.-P. Yang, Y. Xiao, Y.-H. Deng, S. Duhm, N. Ueno, S.-T. Lee, Y.-Q. Li, J.-X. Tang, Electric-field-assisted charge generation and separation process in transition metal oxide-based interconnectors for tandem organic light-emitting diodes. *Adv. Funct. Mater.* **22**, 600–608 (2012).
25. Z. Chen, I. Santoso, R. Wang, L. F. Xie, H. Y. Mao, H. Huang, Y. Z. Wang, X. Y. Gao, Z. K. Chen, D. Ma, A. T. S. Wee, W. Chen, Surface transfer hole doping of epitaxial graphene using MoO$_3$ thin film. *Appl. Phys. Lett.* **96**, 213104 (2010).
26. S. A. O. Russell, L. Cao, D. Qi, A. Tallaire, K. G. Crawford, A. T. S. Wee, D. A. J. Moran, Surface transfer doping of diamond by MoO$_3$: A combined spectroscopic and Hall measurement study. *Appl. Phys. Lett.* **103**, 202112 (2013).
27. M. Tordjman, C. Saguy, A. Bolker, R. Kalish, Superior surface transfer doping of diamond with MoO$_3$. *Adv. Mater. Interfaces* **1**, 1300155 (2014).
28. K. G. Crawford, Enhanced surface transfer doping of diamond by V$_2$O$_5$ with improved thermal stability. *Appl. Phys. Lett.* **108**, 042103 (2016).
29. M. Tordjman, K. Weinfeld, R. Kalish, Boosting surface charge-transfer doping efficiency and robustness of diamond with WO$_3$ and ReO$_3$. *Appl. Phys. Lett.* **111**, 111601 (2017).
30. Z. Yin, M. Tordjman, A. Vardi, R. Kalish, J. A. del Alamo, A diamond:H/WO3 metal–oxide–semiconductor field-effect transistor. *IEEE Electron Device Lett.* **39**, 540–543 (2018).
31. A. Vardi, M. Tordjman, J. A. del Alamo, R. Kalish, A diamond: H/MoO$_3$ MOSFET. *IEEE Electron Device Lett.* **35**, 1320–1322 (2014).
32. M. Vasilopoulou, The effect of surface hydrogenation of metal oxides on the nanomorphology and the charge generation efficiency of polymer blend solar cells. *Nanoscale* **6**, 13726–13739 (2014).
33. M. Vasilopoulou, A. Soultati, D. G. Georgiadou, T. Stergiopoulos, L. C. Palilis, S. Kennou, N. A. Stathopoulos, D. Davazoglou, P. Argitis, Hydrogenated under-stoichiometric tungsten oxide anode interlayers for efficient and stable organic photovoltaics. *J. Mater. Chem. A* **2**, 1738–1749 (2014).
34. I. Kostis, N. Vourdas, G. Papadimitropoulos, A. Douvas, M. Vasilopoulou, N. Boukos, D. Davazoglou, Effect of the oxygen sub-stoichiometry and of hydrogen insertion on the formation of intermediate bands within the gap of disordered molybdenum oxide films. *J. Phys. Chem. C* **117**, 18013–18020 (2013).
35. W. Xie, M. Su, Z. Zheng, Y. Wang, L. Gong, F. Xie, W. Zhang, Z. Luo, J. Luo, P. Liu, N. Xu, S. Deng, H. Chen, J. Chen, Nanoscale insights into the hydrogenation process of layered α-MoO$_3$. *ACS Nano* **10**, 1662–1670 (2016).
36. H. Cheng, M. Wen, X. Ma, Y. Kuwahara, K. Mori, Y. Dai, B. Huang, H. Yamashita, Hydrogen doped metal oxide semiconductors with exceptional and tunable localized surface plasmon resonances. *J. Am. Chem. Soc.* **138**, 9316–9324 (2016).
37. A. Borgschulte, O. Sambalova, R. Delmelle, S. Jenatsch, R. Hany, F. Nüesch, Hydrogen reduction of molybdenum oxide at room temperature. *Sci. Rep.* **7**, 40761 (2017).
38. X. Zhou, H.-Y. Zhou, T.-Y. Cheang, Z.-W. Zhao, C.-C. Shen, K. Liang, Y.-N. Liu, Z.-K. Yang, M. Imran, A.-W. Xu, Monodisperse Pd nanotetrahedrons on ultrathin MoO$_{3-x}$ nanosheets as excellent heterogeneous catalyst for chemoselective hydrogenation reactions. *J. Phys. Chem. C* **121**, 27528–27534 (2017).
39. W. J. Dong, J. Ham, G. H. Jung, J. H. Son, J.-L. Lee, Ultrafast laser-assisted synthesis of hydrogenated molybdenum oxides for flexible organic solar cells. *J. Mater. Chem. A* **4**, 4755–4762 (2016).
40. M. F. J. Vos, B. Macco, N. F. W. Thissen, A. A. Bol, W. M. M. Kessels, Atomic layer deposition of molybdenum oxide from (N^{t}Bu)$_2$(NMe$_2$)$_2$Mo and O$_2$ plasma. *J. Vac. Sci. Technol. A* **34**, 01A103 (2016).
41. A. Bertuch, L. Lecordier, M. Dalberth, G. Sundaram, J. Becker, E. Deguns, M. Saly, D. Moser, R. Kanjolia, Atomic layer deposition of molybdenum oxide using bis(*tert*-butylimido)bis(dimethylamido) molybdenum. *J. Vac. Sci. Technol. A* **32**, 01A119 (2014).
42. M. Diskus, O. Nilsen, H. Fjellvåg, Growth of thin films of molybdenum oxide by atomic layer deposition. *J. Mater. Chem.* **21**, 705–710 (2011).
43. Y. Mori, H. Kawarada, A. Hiraki, Properties of metal/diamond interfaces and effects of oxygen adsorbed onto diamond surface. *Appl. Phys. Lett.* **58**, 940 (1991).
44. M. T. Greiner, L. Chai, M. G. Helander, W.-T. Tang, Z.-H. Lu, Transition metal oxide work functions: The influence of cation oxidation state and oxygen vacancies. *Adv. Funct. Mater.* **22**, 4557–4568 (2012).
45. M. Vasilopoulou, A. Douvas, D. Georgiadou, L. Palilis, S. Kennou, L. Sygellou, A. Soultati, I. Kostis, G. Papadimitropoulos, D. Davazoglou, P. Argitis, The influence of hydrogenation and oxygen vacancies on molybdenum oxides work function and gap states for application in organic optoelectronics. *J. Am. Chem. Soc.* **134**, 16178–16187 (2012).
46. J. A. del Alamo, *Integrated Microelectronic Devices: Physics and Modeling* (Pearson Publication, ed. 1, 2017).

Citation: Z. Yin, M. Tordjman, Y. Lee, A. Vardi, R. Kalish, J. A. del Alamo, Enhanced transport in transistor by tuning transition-metal oxide electronic states interfaced with diamond. *Sci. Adv.* **4**, eaau0480 (2018).

Science Advances

Enhanced transport in transistor by tuning transition-metal oxide electronic states interfaced with diamond

Zongyou Yin, Moshe Tordjman, Youngtack Lee, Alon Vardi, Rafi Kalish and Jesús A. del Alamo

ARTICLE TOOLS	http://advances.sciencemag.org/content/4/9/eaau0480
SUPPLEMENTARY MATERIALS	http://advances.sciencemag.org/content/suppl/2018/09/24/4.9.eaau0480.DC1
REFERENCES	This article cites 45 articles, 4 of which you can access for free http://advances.sciencemag.org/content/4/9/eaau0480#BIBL
PERMISSIONS	http://www.sciencemag.org/help/reprints-and-permissions

Use of this article is subject to the Terms of Service